ÉCOLE POLYTECHNIQUE
FÉDÉRALE DE LAUSANNE

Covariance analysis and error measurement characterization of Tokamak equilibrium reconstruction

Giorgia Dellaferrera

École Polytechnique Fédérale de Lausanne

Table of contents

Introduction

The covariance analysis of a vector of parameters allows, through the derivation of a covariance matrix, to study how a variation of each of the parameters reflects on the values of the other ones. A covariance analysis is applied to the regression involved in the Tokamak equilibrium reconstruction in order to compute a distribution of the plasma current density on the basis of experimental measurements. The covariance matrix found for the free parameters shows to which extent the current sources (external coils, vacuum vessel and plasma current distribution) and the vertical displacement can influence each other, thus indicating to what degree parameters could be considered reliable when a variation of another parameter occurs. Furthermore, the covariance analysis is extended to investigate the interdependence of parameters derived from the free parameters mentioned above, for instance the coordinates of the active point and of the magnetic axis.

The covariance analysis is carried out on the shot 56000 at time t=1s, characterized by a single X point configuration, and on the shot 50765 at time t=0.8s, where a snowflake divertor configuration is present.

1 Covariance analysis in multivariable linear regression

The multivariable linear regression allows to model the relationship between a dependent variable Y and a set of explanatory variables X_i, assuming a linear relationship through the parameters β_i. The formal model can be written as :

$$Y = f(X_1, ..., X_n) = \beta_1 X_1 + \beta_2 X_2 + ... + \beta_n X_n \tag{1}$$

This expression describes how the variable Y changes with the explanatory variables. The observed values Y vary about their mean response, thus the multiple regression model should include a term for this variation : the residual term ϵ.

$$Y = f(X_1, ..., X_n) + \epsilon = \beta_1 X_1 + \beta_2 X_2 + ... + \beta_n X_n + \epsilon \tag{2}$$

Or, in matrix form :

$$Y = X \cdot \beta + \epsilon \tag{3}$$

The terms $\beta_i X_i$ represent the systematic components, while ϵ is the only random variable of the model. The following assumptions are made for ϵ :

1. independence of errors : the residuals should be uncorrelated $\text{covar}(\epsilon_i, \epsilon_j) = 0$
2. homoscedasticity : the variance of the errors should be the same across all levels of independent variables, i.e. the residuals do not vary systematically with the predicted values.

Var ($\epsilon|X_1, \ldots, X_n$) = Var (ϵ) = σ^2I
or
Var ($\epsilon_i|X_1, \ldots, X_n$) = Var (ϵ_i) = σ^2, with i = 1,...,n

3. normality : variables are distributed according to a distribution with zero mean, and consequently also the errors are characterized by a distribution with zero mean
$\epsilon \sim F(\mu = 0)$

1.1 Derivation of covariance matrix for β

The aim of this section is to find the covariance matrix describing the interdependence among the components of the regression vector β.
In multivariable linear regression, the covariance matrix of the estimated parameters is obtained by exploiting the method of least squares.
Regarding the notation, β will denote the vector containing the error and the exact values for the parameters, while $\widehat{\beta}$ will refer to the estimate of these parameters which gives the lowest error :

$$\widehat{\beta} = \underset{\beta}{argmin} ||Y - X \cdot \beta||_2^2 \tag{4}$$

Such estimate is found by exploiting the method of least squares, starting from the definition of residual of a multivariable linear regression :

$$\chi^2 = \sum_{i=1}^{N} \epsilon_i = ||Y - X \cdot \beta||_2^2 \tag{5}$$

where the sum runs over the N measurements, i.e. the dimension of Y.
Developing this definition leads to :

$$\chi^2 = Y^T \cdot Y - 2 \cdot \beta^T \cdot X^T \cdot Y + \beta^T \cdot X^T \cdot X \cdot \beta \tag{6}$$

Finding the estimate $\widehat{\beta}$, requires the first derivative of χ^2 with respect to β to be zero :

$$\frac{d\chi^2}{d\beta} = -2 \cdot X^T \cdot Y + 2 \cdot X^T \cdot X \cdot \widehat{\beta} = 0 \tag{7}$$

from which the estimate of β is found to be

$$\widehat{\beta} = (X^T \cdot X)^{-1} (X^T \cdot Y) \tag{8}$$

The covariance matrix of the estimator $\widehat{\beta}$, whose components are by definition

$$covar(\beta_i, \beta_j) = E[(\beta_i - \widehat{\beta_i}) \cdot (\beta_j - \widehat{\beta_j})] \tag{9}$$

can be found by exploiting equation 8 and the properties for the variance of a linear combination :

$$\begin{aligned} covar(\widehat{\beta}) &= covar((X^T \cdot X)^{-1}(X^T \cdot Y)) = \\ &= (X^T \cdot X)^{-1} X^T \cdot covar(Y) \cdot X (X^T \cdot X)^{-1} = \\ &= (X^T \cdot X)^{-1} X^T \cdot \sigma^2 \cdot I \cdot X (X^T \cdot X)^{-1} = \\ &= \sigma^2 \cdot (X^T \cdot X)^{-1} \cancel{(X^T \cdot X)} \cancel{(X^T \cdot X)^{-1}} = \\ &= \sigma^2 (X^T \cdot X)^{-1} \end{aligned}$$

In order to evaluate σ the reasoning starts from the residual.
First of all, it is useful to notice that, as stated in Equation (5), the residual is the sum of the square of all the contributions of errors ϵ_i : in applications it could be required to weight each i^{th} contribution by a coefficient w_i, for example $w_i^* = \frac{1}{\sigma_i^*}$.

$$\chi^2 = \sum_{i=1}^{N} \epsilon_i^2 \cdot w_i^2 = \sum_{i=1}^{N} \frac{\epsilon_i^2}{\sigma_i^2} \tag{10}$$

Secondly, the residual can be separated in the sum of two contributions :

$$\chi^2 = \chi^2_{min} + \chi^2_k \tag{11}$$

where

$$\chi^2_{min} = ||Y - X \cdot \widehat{\beta}||_2^2 \tag{12}$$

$$\chi^2_k = (\beta - \widehat{\beta})^T \cdot X^T \cdot X \cdot (\beta - \widehat{\beta}) \tag{13}$$

While the latter cannot be computed since it contains the difference between the estimate value and the exact, unknowable, value, the former can be determined precisely as its calculation requires only the estimate of the parameters. Therefore, in the mathematical procedure which will be derived, the residual which will be taken into account will be the estimate of the residual, i.e. χ^2_{min}.
Analogously, for the same reason, the analysis which will follow will consider the estimates of the parameters, instead of the exact quantities and measures which cannot be exactly computed.
For example from the definition of variance

$$\sigma^2 = \frac{1}{N-n} ||Y - X \cdot \beta||_2^2 = \frac{\chi^2}{N-n} \tag{14}$$

where n is the dimension of β (number of estimated parameters).
Its estimate is obtained as follows :

$$\widehat{\sigma^2} = \frac{1}{N-n} ||Y - X \cdot \widehat{\beta}||_2^2 = \frac{\chi^2_{min}}{N-n} \tag{15}$$

This reasoning has thus lead to an expression allowing to compute the covariance matrix for the vector β.

1.2 Derivation of covariance matrix for a function of β

The same arguments used to find the covariance matrix between the components of a vector will now be exploited and developed in order to find an expression for the covariance matrix between the components of a function of the same vector Z(β).
The residual for the function $Z(\beta)$ is :

$$\chi^2(Z(\beta)) = ||Z(\beta) - Z(\widehat{\beta})||_2^2 \tag{16}$$

Let us first consider the case in which Z is a linear function of the parameters β, meaning that it is given by multiplying β by a matrix of coefficients $\overline{\overline{K}}$, such that :

$$Z = \overline{\overline{K}} \cdot \beta \tag{17}$$

This allows to write into the expression for the residual :

$$\chi^2(Z(\beta)) = ||\overline{\overline{K}} \cdot \beta - \overline{\overline{K}} \cdot \widehat{\beta}||_2^2 = ||\overline{\overline{K}} \cdot (\beta - \widehat{\beta}||_2^2 \tag{18}$$

The correlation between the components of the linear function is found by using $Z = \overline{\overline{K}} \cdot \beta$ in the definition of correlation :

$$\begin{aligned} covar(Z(\widehat{\beta}_i), Z(\widehat{\beta}_j)) &= E[(Z(\beta) - Z(\widehat{\beta})) \cdot (Z(\beta) - Z(\widehat{\beta}))] = \\ &= E[\overline{\overline{K}}_{il} \cdot (\beta_l - \widehat{\beta}_l) \cdot \overline{\overline{K}}_{jm} \cdot (\beta_m - \widehat{\beta}_m) \end{aligned}$$

For the reasons presented above, we consider the estimate of the covariance since we evaluate the difference between the exact value and the respective estimate :

$$\begin{aligned} \widehat{covar(Z(\widehat{\beta}_i), Z(\widehat{\beta}_j))} &= \overline{\overline{K}}_{il} \cdot \widehat{(\beta_l - \widehat{\beta}_l)} \cdot \widehat{(\beta_m - \widehat{\beta}_m)} \cdot \overline{\overline{K}}_{jm} = \\ &= \overline{\overline{K}}_{il} \cdot \widehat{covar(\widehat{\beta}_{lm})} \cdot \overline{\overline{K}}_{jm} \end{aligned}$$

where Equation (9) as been exploited.
The estimate of the covariance between $Z(\widehat{\beta}))_i$ and $Z(\widehat{\beta}))_j$ is thus :

$$\widehat{covar(Z(\widehat{\beta}_i), Z(\widehat{\beta}_j))} = \overline{\overline{K}}_{il} \cdot \widehat{covar(\widehat{\beta}_{lm})} \cdot \overline{\overline{K}}_{jm} \tag{19}$$

Let us now consider the case in which Z is a generic function of the parameters β.
Since the discrepancy between β and $\widehat{\beta}$ is expected to be small

$$\beta - \widehat{\beta} = \epsilon \tag{20}$$

the function $Z(\beta)$ can be expanded by Taylor expansion around $\widehat{\beta}$ as follows :

$$\begin{aligned} Z(\beta) &= Z(\widehat{\beta} + \epsilon) = Z(\widehat{\beta}) + \nabla Z|_{\widehat{\beta}} \cdot \epsilon = \\ &= Z(\widehat{\beta}) + \nabla Z|_{\widehat{\beta}} \cdot (\beta - \widehat{\beta}) \end{aligned}$$

By replacing this expansion in the definition of variance for Z, and using Equation (15), the estimate for the variance is found to be :

$$\widehat{\sigma(Z(\beta))^2} = \frac{||Z(\beta) - Z(\widehat{\beta})||_2^2}{N-n} =$$
$$= \frac{[\cancel{Z(\widehat{\beta})} + \nabla Z|_{\widehat{\beta}} \cdot \widehat{(\beta - \widehat{\beta})} - \cancel{Z(\widehat{\beta})}]^T \cdot [\cancel{Z(\widehat{\beta})} + \nabla Z|_{\widehat{\beta}} \cdot \widehat{(\beta - \widehat{\beta})} - \cancel{Z(\widehat{\beta})}]}{N-n} =$$
$$= \frac{\nabla Z|_{\widehat{\beta}}^T \cdot \widehat{(\beta - \widehat{\beta})}^T \cdot \widehat{(\beta - \widehat{\beta})} \cdot \nabla Z|_{\widehat{\beta}}}{N-n}$$

Analogously to the case of Z being a linear function, the covariance is found to be :

$$\widehat{covar(Z(\widehat{\beta}_i), Z(\widehat{\beta}_j))} = \nabla Z|_{\widehat{\beta}} \cdot \widehat{covar(\widehat{\beta})} \cdot \nabla Z|_{\widehat{\beta}} \tag{21}$$

2 The LIUQE regression

2.1 Inverse equilibrium reconstruction

Tokamak's plasmas will be described by considering an axisymmetric geometry and the equations describing the ideal Magnetohydrodynamic equilibrium (MHD) under the assumptions of isotropic pressure and no net fluid velocity :

$$\begin{aligned} \mathbf{j} \times \mathbf{B} &= \nabla p \\ \nabla \times \mathbf{B} &= \mu_0 \mathbf{j} \\ \nabla \cdot \mathbf{B} &= 0 \end{aligned} \tag{22}$$

In cylindrical coordinates (r,z,ϕ) the magnetic field can be expressed using the poloidal flux function ψ and T = r B ϕ :

$$\mathbf{B} = -\frac{1}{2\pi r}\frac{\partial \Psi}{\partial z}\nabla r + \frac{1}{2\pi r}\frac{\partial \Psi}{\partial r}\nabla z + T\nabla\phi \tag{23}$$

MHD equations (22) can be combined into a second order differential equation comparable to a Poisson equation :

$$\Delta^* \psi = -2\pi\mu_0 r j_\phi \tag{24}$$

where the elliptical operator Δ^* is defined as :

$$\Delta^* = r(\frac{\partial}{\partial r}) \cdot (r\frac{\partial}{\partial r}) + (\frac{\partial^2}{\partial z^2}) \tag{25}$$

The current density j_ϕ takes the following expression :

$$j_\phi = 2\pi(r\frac{dp}{d\psi} + \frac{T}{\mu_0 r}\frac{dT}{d\psi}) \tag{26}$$

where p and T are arbitrary functions of the poloidal magnetic flux ψ only.
Equations 24 and 25 are combined in order to get the so called **Grad-Shafranov equation**

$$\Delta^*\psi = -4\pi^2\mu_0 r(rp' + \frac{TT'}{\mu_0 r}) \tag{27}$$

The inverse equilibrium reconstruction aims at identifying the functions $p'(\psi)$,$TT'(\psi)$ and $\psi(r,z)$ satisfying the Grad-Shafranov equation which best fit the experimental measurements.
Equation (27) is a non linear equation, since plasma is restricted to the closed magnetic field line region whose boundaries depend on the solution itself. It is solved using an iterative algorithm involving the following equation :

$$\Delta^*\psi^{t+1} = -2\pi^2\mu_0 r \cdot j_\phi^{(t)}(r,\psi^{(t)}) \tag{28}$$

where t represents the iteration number.
At each t^{th} iteration both the boundary region of plasma and the functions describing the plasma current density ($p'^{(t)}(\psi^{(t)})$, $TT'^{(t)}(\psi^{(t)})$) are adjusted in order to best reproduce the measurements. To this aim the latter functions are parametrized as follows :

$$\begin{aligned} p' &= g_p(\psi; a_p) \\ TT' &= g_T(\psi; a_T) \end{aligned} \tag{29}$$

where a_p and a_T are determined on the basis of the fitting criteria and g_p and g_T are chosen in such a way all possible equilibria can be taken into account.
It is convenient to consider only the parametrized functions which are linear combinations of functions $g_g(\psi)$ depending on ψ only. In this case the coefficients a_g are the free parameters of the problem :

$$j_\phi = 2\pi(rp' + \frac{TT'}{\mu_0 r}) = \sum_g a_g r^{\nu_g} g_g(\psi) \tag{30}$$

where

1. ν_g is equal to 1 for the terms contributing to p' and to -1 for those contributing to TT'
2. g_g=0 outside the plasma region Ω_p

The combination of this parametrization with a cost function and with measurements characterized by a linear relationship with p' and TT' leads to a linear regression problem.
Furthermore, the algorithm can be stabilized by introducing a vertical shift in the flux distribution :

$$j_\phi = \sum_g a_g r^{\nu_g} g_g(\psi(r, z + \delta z)) \tag{31}$$

which is valid only if the algorithm converges towards a negligible value of δz . The second step of the iterative inverse equilibrium problem algorithm consists in identifying the free parameters $\{a_g, \delta z\}$ in the parametrization of the plasma current distribution.The source term base functions are often chosen as the three polynomials :

1. for p'

$$\nu_1 = 1, g_1 = (\psi - \psi_0)[(r,z) \in \Omega_p] \tag{32}$$

2. for TT'

$$\begin{aligned} \nu_2 = -1, \quad g_2 = (\psi - \psi_0)[(r,z) \in \Omega_p] \\ \nu_3 = -1, \quad g_3 = (\psi - \psi_0)(\psi - \psi_A)[(r,z) \in \Omega_p] \end{aligned} \tag{33}$$

The value of these functions on the inner computational grid r_y x z_y is stored in the elements of a rectangular matrix $T_{yg} = r_y^{\nu_g} g_g(\psi(r_y, z_y))\Delta r \Delta z$ where Δr,Δz are the grid point spacing.

The available experimental measurements are :

— I_a = active coil currents
— ψ_f = flux loops
— B_m = magnetic probes
— I_s = vacuum vessel currents
— I_p = plasma currents
— ϕ_t = toroidal flux produced by the plasma

The expected value for these measurements can be written as

$$\begin{aligned} \psi_f &= M_{fa} \cdot I_a + M_{fs} \cdot I_s + (M_{fy} \cdot T_{yg}) \cdot a_g + (\partial_{z_f} M_{fy} \cdot I_y)\delta z \\ B_m &= B_{ma} \cdot I_a + B_{ms} \cdot I_s + (B_{my} \cdot T_{yg}) \cdot a_g + (\partial_{z_m} B_{my} \cdot I_y)\delta z \\ I_p &= T_{pg} \cdot a_g \\ \Phi_t &= T_{tg} \cdot a_g \end{aligned}$$

where

— $I_y = j_\phi^{(t-1)}(r_y, z_y)\Delta r \Delta z$
— $T_{pg} = \sum_y T_{yg}$

in which the terms $M_{f(j)}$ and $B_{m(j)}$ are the mutual inductances calculated through Green functions.
The following set of free parameters is introduced :

— J_a = free parameter containing the uncertainty for active coil currents
— J_s = free parameter containing the uncertainty for vacuum vessel currents
— a_g = related to the source function parametrization
— δz = bulk displacement of the plasma column in vertical direction

This allows to formulate the linear regression problem in matrix form as :

$$\begin{bmatrix} \psi_f \\ B_m \\ I_a \\ I_s \\ I_p \\ \phi_t \end{bmatrix} \simeq \begin{bmatrix} M_{fa} & M_{fs} & (M_{fy} \cdot T_{yg}) & \partial_{z_f} M_{fy} \cdot I_y \\ B_{ma} & B_{ms} & (B_{my} \cdot T_{yg}) & \partial_{z_m} B_{my} \cdot I_y \\ I_a & 0 & 0 & 0 \\ 0 & I_s & 0 & 0 \\ 0 & 0 & T_{pg} & 0 \\ 0 & 0 & T_{tg} & 0 \end{bmatrix} \cdot \begin{bmatrix} J_a \\ J_s \\ a_g \\ \delta z \end{bmatrix} \tag{34}$$

This block structure of matrix can be exploited for the resolution methods, and the dependent parameters can be rewritten, in a weighted version, as :

$$Y_d = \begin{bmatrix} w_f \psi_f \\ w_m B_m \\ w_a I_a \\ w_s I_s \\ w_p I_p \\ w_t \phi_t \end{bmatrix} \tag{35}$$

where the weighting w_i are inversely proportional to the associated measurement errors, thus $w_i^* = \sigma_i^{*-1}$.
The free parameters are written as :

$$a_G = \begin{bmatrix} J_a \\ J_s \\ a_g \\ \delta z \end{bmatrix} \tag{36}$$

The two vectors are related by the matrix of coefficients AdG, containing the weighted version of the explanatory variables such that the following relationship holds :

$$Y_d = AdG \cdot a_G + \epsilon \tag{37}$$

3 Results

The covariance analysis technique discussed in chapter 1 is applied to the multivariable regression expressed by Equation (37). At first the covariance matrix for the vector a_G is computed and is then employed to calculate the error in the total energy of the system. Furthermore the covariance matrix for the coordinates of both the X point and the magnetic axis position is found and is used to compute the error on the positions.

3.1 Results of the covariance analysis

The covariance matrix for the estimate of the free parameters of the a_G vector is calculated, as explained in section 1.1, as :

$$covar(\widehat{a_G}) = \sigma^2 \cdot (AdG^T \cdot AdG)^{-1} \tag{38}$$

The diagonal of the covariance matrix, containing the variances of each parameters computed for the shot 56000 at time 1s, is reported, along with the estimated values for a_G, in Table 1. As shown in the table, δz exhibits a variance of the order of $3 \cdot 10^{-5} m^2$, corresponding to an error of the order of few millimeters.
The covariance matrix obtained for the vector a_G is graphically displayed, in its normalized version

$$covar(a_{Gi}, a_{Gj}) = \frac{covar(a_{Gi}, a_{Gj})}{\sqrt{(covar(a_{Gi}, a_{Gi})) \cdot (covar(a_{Gj}, a_{Gj}))}} \tag{39}$$

in order to give an immediate perception of the degree of correlation among the parameters. The plot for the shot 56000 at time 1 s is shown in Figure 1.

Since the matrix is normalized, all the diagonal terms, representing the correlation of each parameter with its self, are equal to one. The off diagonal terms represent instead the correlation between the parameters. The strongest correlations are found to be among the parameters describing the basis functions (correlation coefficient of magnitude of the order of 0.94 to 0.99, positive or negative depending on the specific terms).

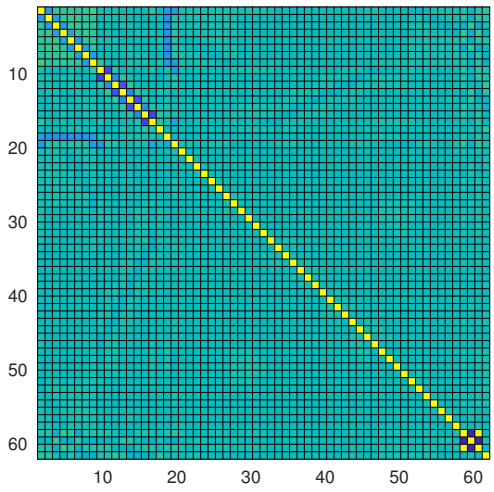

Figure 1. Normalized covariance matrix for shot 56000 at time 1s

Also the coil currents, in particular the F currents represented by the terms 9^{th} to 15^{th}, show high correlation values (negative correlation coefficient, with a magnitude between 0.4 to 0.7) when adjacent, i.e. the 10^{th} with the 9^{th} and the 11^{th}, the 11^{th} with the 10^{th} and the 12^{th}, etc. This behaviour is due to the geometry of the TCV : these currents, indeed, flow in coils which are close in space, and thus produce similar response in the measurements.
Furthermore, the term 18^{th}, describing the ohmic heating coil currents, is found to be significantly correlated (the correlation coefficient is approximately 0.35) to the first eight terms, which are the E coil currents. This can be similarly explained, by considering that these coils are physically close.

3.2 Use of the covariance matrix to compute the error on the kinetic energy

The covariance matrix in Equation (38) has been used in order to compute the error on the total kinetic energy due to the correlation among the basis functions a_g.
The total kinetic energy, calculated to be $W_k = 2.4 \cdot 10^3$ J, indeed, depends on the a_g parameters through the coefficients contained in the matrix W_{kg} :

$$W_k = W_{kg} \cdot a_g \tag{40}$$

Therefore, as stated in Equation 19, the error on the total kinetic energy can be expressed as :

$$\sqrt{\sigma^2} = \sqrt{W_{kg} \cdot cov(a_g) \cdot W_{kg}} = 3 \cdot 10^3 J \tag{41}$$

where the covariance matrix for the parameters a_g has been build by extracting the entries of $\mathrm{cov}(a_G)$ relative to the basis functions only.
In conclusion, the error is found to be of the same order of magnitude of the energy value, thus the value obtained for the kinetic energy is affected by a large error if three basis functions are used.

3.3 Derivation of covariance matrix for the coordinates of X point and of magnetic axis

The active (X) point is the site at which two magnetic flux lines intersect, as shown in Figure 2.

Being solenoidal, the magnetic field vanishes at the X point. Therefore the active point corresponds to the position at which the gradient of the magnetic flux is null. Therefore a possible inaccuracy on the gradient of the flux gives rise to an imprecision on the determination of the position.
Also the calculation of the position of the magnetic axis depends on the gradient of the magnetic flux, since on the magnetic axis the magnetic field vanishes and so does the gradient of the magnetic

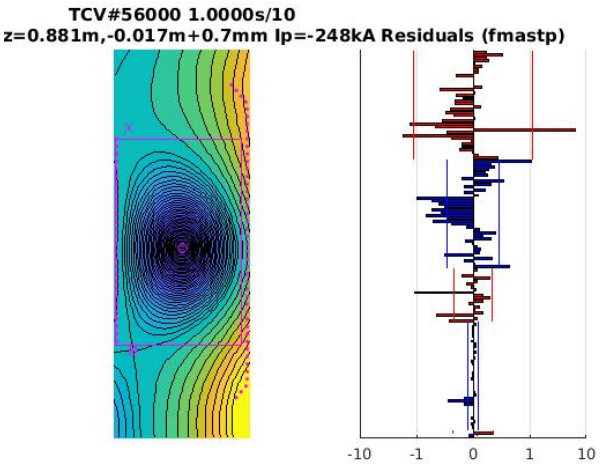

Figure 2. X point for shot 56000 at time 1s

Table 1. Estimated value, standard deviation and relative error for aG parameters

		Estimated value for a_G	**Standard deviation for a_G**	**Relative error (σ/a_G)**
COIL CURRENTS J_a	1	-1052.18587125039	113.951097436285	0.108299398946376
	2	-308.794061296791	122.982405587205	0.398266744738341
	3	1828.36887542333	124.761714610255	0.0682366213335194
	4	3286.73698432724	125.435946123067	0.0381642786511993
	5	3242.85578715039	124.656391202957	0.0384403129170589
	6	982.222732219832	124.464390932547	0.126717074294601
	7	452.853939867304	122.998649650309	0.271607772003375
	8	323.918713551730	113.487174229443	0.350356955252968
	9	1707.14428579843	107.679523201323	0.0630758185450985
	10	2193.13763003111	106.507076601744	0.0485637905908503
	11	87.7324492097152	99.5054046395454	1.13419157376637
	12	418.130920908296	99.2408824045733	0.237344040926212
	13	998.317350619046	99.1881026801161	0.0993552827851891
	14	886.711432404631	99.5522393141876	0.112271293316041
	15	817.089322924804	107.153459894173	0.131140448036468
	16	740.000814160315	109.567934311361	0.148064613193282
	17	-195.893072062524	160.869860743998	0.821212608747350
	18	-1494.82950863181	130.722848381016	0.0874500052522144
VESSEL CURRENTS J_S	19	-1308.61963633141	110.263762859406	0.0842595967522848
	20	-939.539440559538	180.357068679626	0.191963275721789
	21	-932.825467009925	180.303224825922	0.193287202378668
	22	-782.396323242884	180.242344668224	0.230372177518874
	23	-717.162623027474	180.269951801761	0.251365514617533
	24	-927.420946257248	180.378195220776	0.194494415883877
	25	-778.800964441537	180.210128083055	0.231394330915191
	26	-656.644144459518	180.182657230975	0.274399244630869
	27	-727.251032452511	179.958559655165	0.247450401064801
	28	-854.466189466694	179.420737181945	0.209979914236195
	29	-730.102605875473	179.581505110170	0.245967489589812
	30	-717.720088375216	179.654889706544	0.250313308233088
	31	-660.443394920557	179.651090212082	0.272015878414064
	32	-641.533457517299	179.563404756381	0.279897178630842
	33	-814.390179959591	180.110642922552	0.221160135957790
	34	-776.959377310841	180.177678012349	0.231901027613526
	35	-608.465620482548	179.934881507717	0.295719060289747
	36	-545.855660202100	180.093254786332	0.329928345379168
	37	-487.285068977300	180.024532379711	0.369443974053097
	38	-351.499404211316	180.089862137220	0.512347560136839
	39	-427.830186114911	179.912675062857	0.420523564960735
	40	-388.399423911562	180.089899276132	0.463671901112651
	41	-372.970785082745	180.024469047227	0.482677132492530
	42	-392.627877756972	180.093226091268	0.458686803189103
	43	-471.296924886217	179.933764532437	0.381784295698254
	44	-353.446287855450	180.175252033885	0.509766994943153
	45	-405.155648634414	180.097084352748	0.444513324594557
	46	-421.930841218482	179.546084947183	0.425534394282904
	47	-472.569801481780	179.214248920376	0.379233392312492
	48	-639.196315086703	179.168303819866	0.280302466692980
	49	-757.848261234820	179.252657877438	0.236528427980250
	50	-841.931431404381	179.412643474270	0.213096502615422
	51	-924.004730454132	179.965811985643	0.194767197671373
	52	-910.908608717401	180.182688453902	0.197805451314822
	53	-891.552800293966	180.210476650249	0.202131019711709
	54	-589.771298157936	180.377987757351	0.305843957345390
	55	-731.827610905375	180.273442004777	0.246333206507135
	56	-801.815230170376	180.241433894997	0.224791731452517
BASIS FUNCTIONS a_g	57	-779.132908299435	180.306342264582	0.231419235850434
	58	536.442285171931	672.287587710871	1.25323377051718
	59	5629.91106650464	2080.97801448557	0.369628931949996
	60	-17291.5263840916	16119.7661732183	0.932235004311052
δz	61	0.000666117422110336	0.00549686559524336	8.25209702191644

flux. As for the X point
case, we can relate the propagation of error on the gradient to the error on the axis position.
The result expressed in Equation (19) leads to the 2 x 2 covariance matrix describing the interdependence of the gradient of the flux along the r and z direction :

$$covar(\frac{\partial \Psi}{\partial r}, \frac{\partial \Psi}{\partial z}) = \overline{\overline{F}} \cdot \widehat{covar(a_G)} \cdot \overline{\overline{F^T}} \tag{42}$$

where $\overline{\overline{F}}$ is the matrix relating the a_G coefficients to the derivative of the flux, i.e. satisfying :

$$(\frac{\partial \Psi}{\partial r}, \frac{\partial \Psi}{\partial z}) = \overline{\overline{F}} \cdot a_G \tag{43}$$

This matrix is obtained by first expressing the flux at the X point (or magnetic axis) position as a function of the free parameters, on the basis of equation (34) :

$$\Psi_x = M_{xa} J_a + M_{xs} J_s + (M_{xy} \cdot T_{yg}) a_g + (\partial M_{xy} \cdot I_y) \delta z \tag{44}$$

Then the gradient components of Ψ_x are derived :

$$\begin{pmatrix} \partial_r \Psi \\ \partial_z \Psi \end{pmatrix} = \begin{pmatrix} \partial_r M_{xa} & \partial_r M_{xs} & \partial_r M_{xy} \cdot T_{yg} & \partial_r \partial_z M_{xy} \cdot I_y \\ \partial_z M_{xa} & \partial_z M_{xs} & \partial_z M_{xy} \cdot T_{yg} & \partial_r \partial_z M_{xy} \cdot I_y \end{pmatrix} \cdot a_G = \overline{\overline{F}} \cdot a_G \tag{45}$$

in which the expression for $\overline{\overline{F}}$ is found.
In order to find the position of the X point (or magnetic axis), or, more precisely, the change of this position when the gradient of the flux is considered to change, one can approximate the flux near the nominal X point position (r_X , z_X) by a second order expansion

$$\Psi(r,z) \cong \Psi_x + (r - r_x, z - z_x) \nabla \Psi_x + \frac{1}{2} \cdot (r - r_x, z - z_x) \cdot H \cdot (r - r_x, z - z_x)^T \tag{46}$$

where the Hessian matrix is explicitly

$$H = \begin{bmatrix} \dfrac{\partial^2 \Psi}{\partial r^2} & \dfrac{\partial^2 \Psi}{\partial r \partial z} \\ \dfrac{\partial^2 \Psi}{\partial z \partial r} & \dfrac{\partial^2 \Psi}{\partial z^2} \end{bmatrix} \tag{47}$$

The expression for the gradient of the flux follows :

$$\nabla \psi(r,z) = \nabla \psi_x + H(r - r_x, z - z_x)^t \tag{48}$$

Since the gradient is zero at the X point ($\nabla \psi_x = 0$) and the variation in the nominal position can be calculated with

$$\begin{pmatrix} r - r_x \\ z - z_x \end{pmatrix} = H^{-1} \nabla \psi \tag{49}$$

Being the error on the coordinates along the two directions a linear function of the gradient of the flux through the matrix H^{-1}, by exploiting Equation (19) the covariance matrix describing the interdependence of the coordinates r and z (both for the X point and for the magnetic axis position) can be written as :

$$covar(\Delta r, \Delta z) = H^{-1} \cdot covar(\frac{\partial \Psi}{\partial r}, \frac{\partial \Psi}{\partial z}) \cdot H^{-1} \tag{50}$$

3.4 Results of the covariance analysis for the X point position

The described algorithm has lead to two types of representations of errors.

1. Firstly the uncertainty on the coordinates has been found as error bars orientated along the r and z direction.
   Analogously to the case of total kinetic energy, Equation 19 is used and the error on the gradient along the radial and vertical directions is computed through :

$$\begin{aligned} \Delta \frac{\partial \Psi}{\partial r} &= \sqrt{\overline{\overline{F}}_r \cdot cov(a_G) \cdot \overline{\overline{F}}_r^T} \\ \Delta \frac{\partial \Psi}{\partial z} &= \sqrt{\overline{\overline{F}}_z \cdot cov(a_G) \cdot \overline{\overline{F}}_z^T} \end{aligned} \tag{51}$$

   where $\overline{\overline{F}}_r$ and $\overline{\overline{F}}_z$ are the matrices given in Equation (45). The error on the coordinate along r and z is found by dividing the error on the gradient by the second derivative of the flux in the respective direction :

$$\begin{aligned} \Delta r &= \frac{\Delta \frac{\partial \Psi}{\partial r}}{\frac{\partial^2 \Psi}{\partial r^2}} \\ \Delta z &= \frac{\Delta \frac{\partial \Psi}{\partial z}}{\frac{\partial^2 \Psi}{\partial z^2}} \end{aligned} \tag{52}$$

   The obtained results are :

   — $\Delta r = 1.84$ cm
   — $\Delta z = 1.71$ cm

2. Secondly, the covariance analysis allows to treat the uncertainty along the two directions simultaneously. Indeed, since the off diagonal terms of the covariance matrix relating the radial and the vertical position are not null, one could infere that the errors on the two directions are interdependent. The diagonalization leading to the eigenvectors and eigenvalues of the covariance matrix allows to compute the parameters needed to represent an ellipse of confidence. The axis of the ellipse are orientated with an angle $\theta = 0.13\pi$ with respect to the r or z axis. The lengths of the axis are :

— axis 1 = 0.29 cm
— axis 2 = 0.65 cm
It is possible to notice a net discrepancy between the values found for the length of the axis and the size of the error bars not taking the covariance into account. Since the former analysis is more accurate, the results obtained for the ellipses are considered to be the most reliable.

In order to find how much the uncertainty on the vertical displacement of plasma δz affects the error on both the vertical and radial position error, the same algorithm is applied a second time imposing the contribution of δz to be null. This is done by substituting the coefficients multiplying the contribution of the δz with zeros.
The obtained results for the length of the ellipse's axis are :

— axis 1 = 0.27 cm
— axis 2 = 0.57 cm
A comparison between the results obtained in the two cases shows immediately, as expected, that adding the δz contribution affects only very slightly (0.04%)the error on the radial position (non null,however, since the covariance is non null), while it results into a more consistent contribution to the inaccuracy on the vertical position (0.14%).

3.5 Results of the covariance analysis for the magnetic axis position

Analogously to case of the active point, the two representations of errors are obtained.

1. Uncertainty as magnitude of the error bars :

   — $\Delta r = 0.09$ cm
   — $\Delta z = 0.32$ cm
2. Uncertainty represented by an ellipse of confidence characterized by :
   — axis 1 = 0.08 cm
   — axis 2 = 0.33 cm
   — $\theta = 0.05\pi$
   It is possible to see that the length of the axis differs only slightly from the error bars size of point 1.

3.6 Results of the covariance analysis for a snow flake divertor

The introduction of the Hessian matrix allows one to employ the described algorithm also in the case of a snow flake divertor. The snowflake magnetic configuration, as shown in Figure 3, occurs when two null poloidal fields, located very closely in space create a hexagonal structure.

In this configuration the second derivatives of the flux in both the radial and vertical directions are null. Therefore computing the total error on the coordinates as

— $\Delta r = \dfrac{\Delta \dfrac{\partial \Psi}{\partial r}}{\dfrac{\partial^2 \Psi}{\partial r^2}}$

— $\Delta z = \dfrac{\Delta \dfrac{\partial \Psi}{\partial z}}{\dfrac{\partial^2 \Psi}{\partial z^2}}$

is not possible since it would imply dividing by a null quantity.
Instead since the covariance cov(Δ r,Δz) is non zero, the Hessian matrix will have non null off-diagonal terms, which allows to obtain a finite result by applying Equation (50).
The snowflake divertor configuration has been obtained during the shot #50765 at time 0.8s.
The results for the length of the axis of the error ellipse and their orientation angle are summarized in Table 1.

	X point 1	angle θ_1	X point 2	angle θ_2	Magnetic axis	angle $\theta_{m.a.}$
Axis 1	4.34 cm	0.12π	5.23 cm	0.41π	0.59 cm	0.16π
Axis 2	2.14 cm		2.60 cm		3.31 cm	

According to these results, the error on the coordinates for the snowflake configuration is approximately one order of magnitude higher than for a single X point situation.

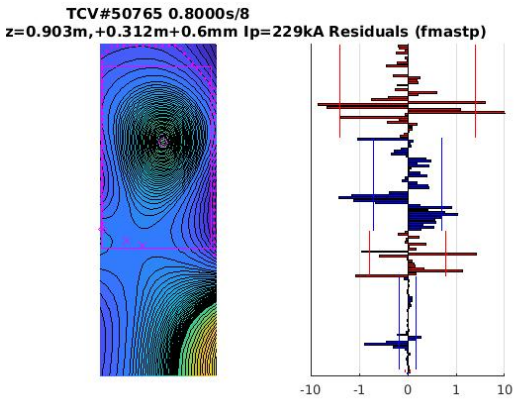

Figure 3. X point for shot 50765 at time 0.8s

4 Measurement error characterization

The data collected for the shots ranging from #50000 to #58000 with sample times 0s to 2s every 100ms is analyzed in order to investigate the error distribution for the poloidal magnetic field and poloidal current.
In section 1 the hypothesis that the error calculated as the difference between the measurement and the fit for a given quantity was distributed according to a distribution function with $\mu = 0$ was made.
However the experimental errors for both the poloidal magnetic field and the poloidal current for the considered samples have a non zero mean. The possible sources of errors are investigated.

4.1 Error in poloidal magnetic field

Error in the compensation of the toroidal parasitic contribution One of the main sources of errors is due to the parasitic coupling of the probes to the toroidal magnetic field. Indeed, the probes measuring the poloidal magnetic field are affected by a coupling with the toroidal field, which adds to the measurements a contribution proportional to the toroidal magnetic field. This investigation starts from the hypothesis that the parasitic error depends only on the toroidal field and not on the poloidal field. Under this assumption the model for the measurement of the poloidal field can be described by :

$$X = A_p B_p + \epsilon_\phi = A_p B_p + A_\phi B_\phi \tag{53}$$

where X is the measured value, B_p is the poloidal field and B_ϕ is the toroidal field. Furthermore A_p is the coefficient of the poloidal field value in the measurement, which is expected to be close to 1, and A_ϕ is the coefficient that introduces parasitic coupling.
This contribution does not affect the values obtained through fitting (B_{fit}), thus can be detected by subtracting the fitted values to the measured ones :

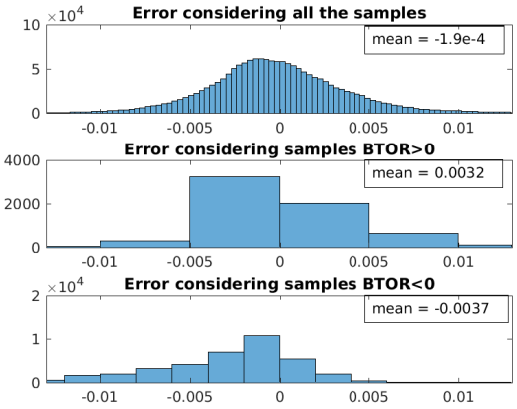

Figure 4. Error distribution for all the probes

$$\epsilon_\phi = X - B_{fit} \tag{54}$$

By considering separately the samples obtained with positive and negative values of the toroidal magnetic field, it is found that the mean of the distribution of errors is positive and negative respectively when the toroidal field is positive and negative. Since the number of samples characterized by negative toroidal field (N_{pos} = 1447174) is much greater than those characterized by positive field (N_{neg} = 242514), the mean over all the samples results to be negative. The measurements have been divided in two classes only since the values of the toroidal field are concentrated around two values, one positive (rB_ϕ = 1.26 Tm) and one negative (rB_ϕ = -1.29 Tm).
The histograms for the distribution of error concerning all the probes for the two classes are displayed in Figure 4.
The same procedure consisting in dividing the measurements into two classes has been applied probe by probe. Depending on the probe and on its coupling with respect to the magnetic field, the distribution of the errors exhibits a mean value which is in general dependent on the sign of the toroidal field. Four cases are possible :

1. The mean is positive for positive values of B_ϕ and negative for negative values of B_ϕ ; this is the case of probe 9, reported in Figure 5
2. The mean is negative for positive values of B_ϕ and positive for negative values of B_ϕ ; this is the case of probe 15, reported in Figure 6
3. The mean is positive for both classes of the B_ϕ ; this is the case of probe 21, reported in Figure 7
4. The mean is negative for both classes of the B_ϕ ; this is the case of probe 32, reported in Figure 8

Concerning the first two cases, the histograms show a clearly different trend for the error according to the two values of the toroidal fields. This is already evident from the distribution of errors taking into account all the sample, which is indeed characterized by two peaks, the higher corresponding to the samples obtained with $B_\phi < 0$ and the lower to those with $B_\phi > 0$. As for probe 9 and probe 15, instead, such a separation is not so distinct.
A connection between this findings and the results obtained through linear regression will be presented in the Section **Estimation of A_p and A_ϕ through regression**.

Error in the calibration The model in Equation (53) assumes that the only source of inaccuracy is due to the parasitic coupling with the toroidal field. In reality, measurements are affected also by an error in the calibration which results into an error proportional to the poloidal magnetic field. This calibration error could be attributable, for instance, to an inaccuracy in the probe effective area or in the electronic gain.
The hypothesis that the parasitic error $\epsilon_\phi = A_\phi B_\phi$ depends on the toroidal field only is still considered valid. Under this assumption, the model taking into account this second source of error can be written as :

$$X = (A_p + \epsilon_{cal})B_p + A_\phi B_\phi \tag{55}$$

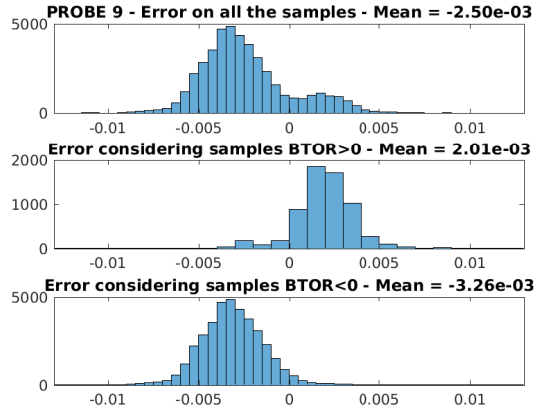

Figure 5. Error distribution as function of Bϕ for **probe 9**

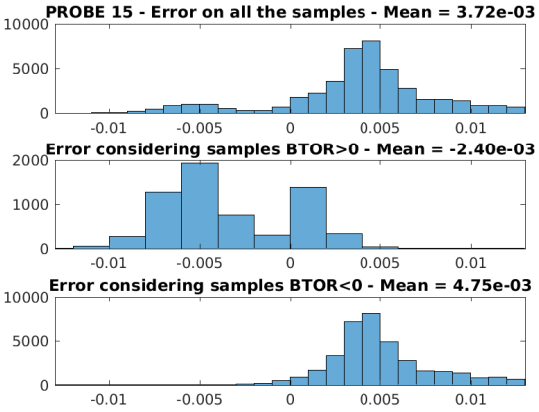

Figure 6. Error distribution as function of Bϕ for **probe 15**

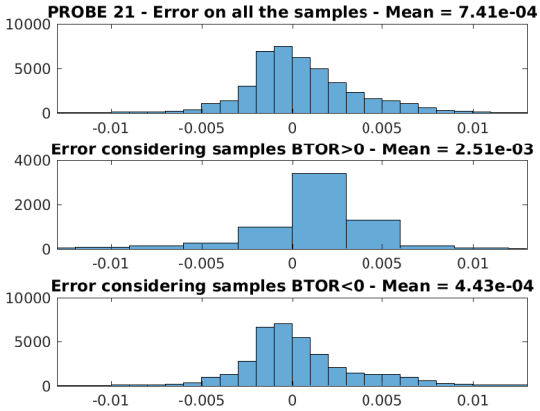

Figure 7. Error distribution as function of Bϕ for **probe 21**

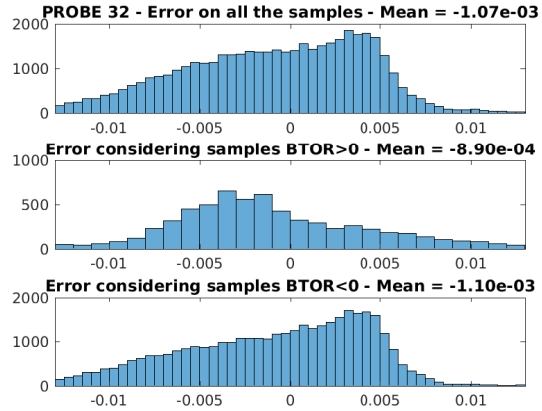

Figure 8. Error distribution as function of Bϕ for **probe 32**

In order to analyze the calibration error, the samples have been divided, probe by probe, in different classes according to the value of the poloidal field. Each class is associated to a range of the poloidal field such that a sufficient number of measurement falls in it. As many as seven ranges have been chosen for each probe : indeed, contrary to the toroidal field, the poloidal field has a continuous distribution, which causes the division into two classes, one positive and one negative, to be meaningless. Furthermore, in order to render the parasitic error negligible, for each probe the values have been divided previously according to the sign of the toroidal field. Since data are mainly available for measurements with negative toroidal field, the dependence of the error distribution on the poloidal field is investigated by selecting the shots performed with negative B_ϕ. The error, therefore, has been detected, similarly to the parasitic error case, by subtracting the fitted values to the exponential values, considering only the measurements for which $B_\phi < 0$:

$$\epsilon_p = X|_{B_\phi<0} - B_{fit} \tag{56}$$

The ranges fixed for B_p are different for each probe since, depending on the position of the probe, the magnitude of B_p can be different.
Four probes are investigated in detail : probes number 7, 35, 28 and 32. For each of the probe a histogram showing the distribution and its mean for the different ranges is displayed together with a plot for the behaviour of mean and variance of the error as a function of the poloidal field. Probes 7, 35 and 32 show a linearly decreasing behaviour as a function of B_p. The data are fitted with a straight line, which is superimposed in red on the graphs of the mean in the figures 9, 10 and 14. The found linearly decreasing behaviour is consistent with the model in equation (55) which involves an error linear in B_p. The slope of the fitted line therefore corresponds to ϵ_{cal}. It should also be noticed that the fitted line does not intercept the x axis in the point corresponding to $B_p = 0$ but it exhibits an offset. In Table 2 the obtained results for the calibration error and for the offset for the three examined probes are reported.
Regarding the variance the peaks which are at the edge of the graphs can be

Table 2. ϵ_{cal} values obtained through fitting of $\mu(B_{pol})$

# probe	ϵ_{cal}	offset
7	$-2.28 \cdot 10^{-2}$	$-1.23 \cdot 10^{-3}$
35	$-3.43 \cdot 10^{-2}$	$-2.72 \cdot 10^{-4}$
32	$-4.87 \cdot 10^{-3}$	$-1.34 \cdot 10^{-3}$

explained by the fact that in the ranges corresponding to the far tails of the distribution there are less measurements on which the average is performed.

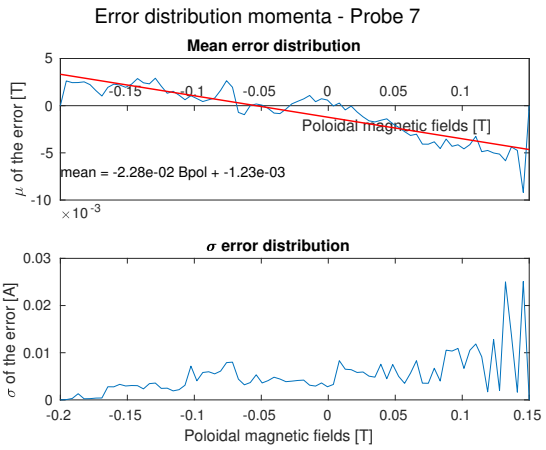

Figure 9. Error distribution as function of B_p for **probe 7**

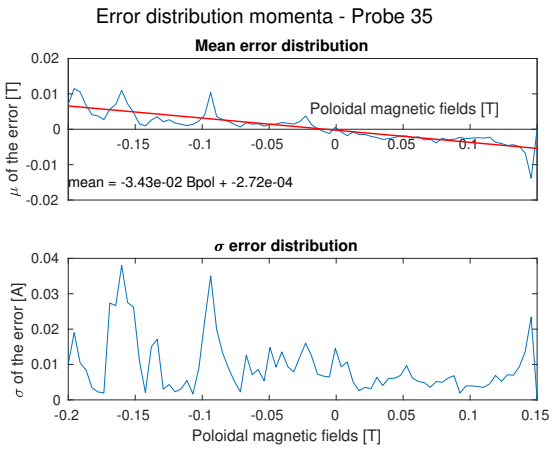

Figure 10. Error distribution as function of B_p for **probe 35**

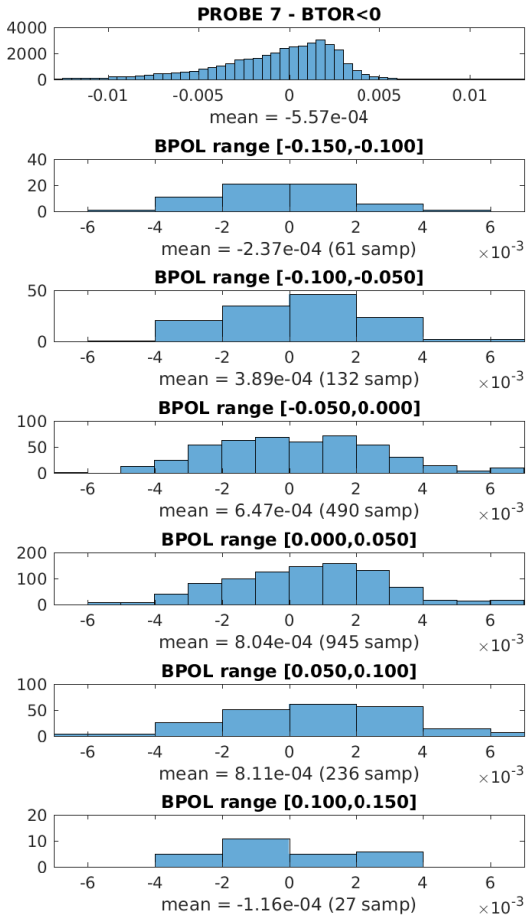

Figure 11. Error distribution as function of B_p for **probe 7**

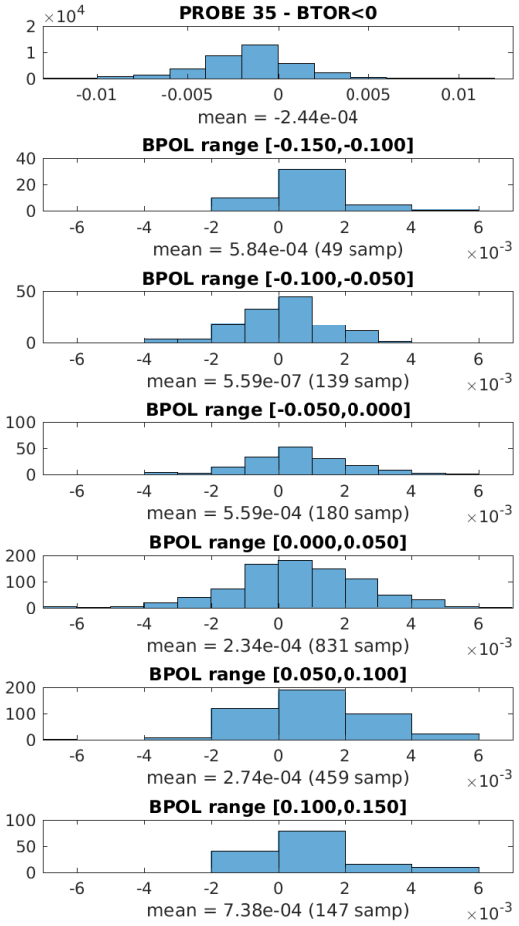

Figure 12. Error distribution as function of B_p for **probe 35**

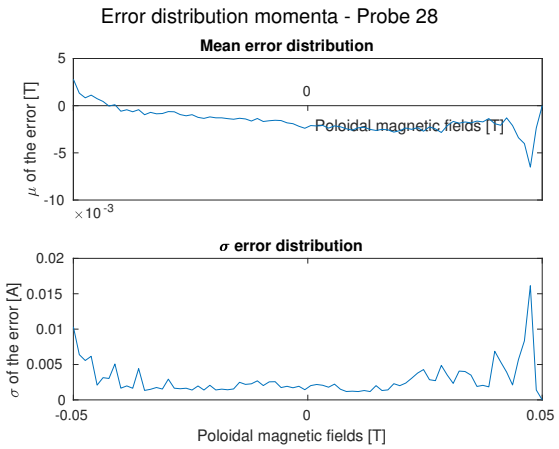

Figure 13. Error distribution as function of B_p for **probe 28**

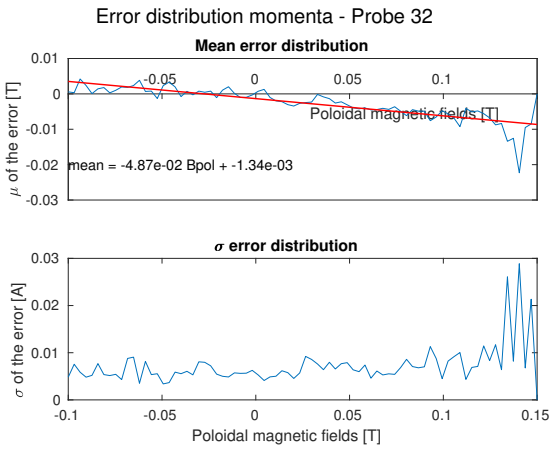

Figure 14. Error distribution as function of B_p for **probe 32**

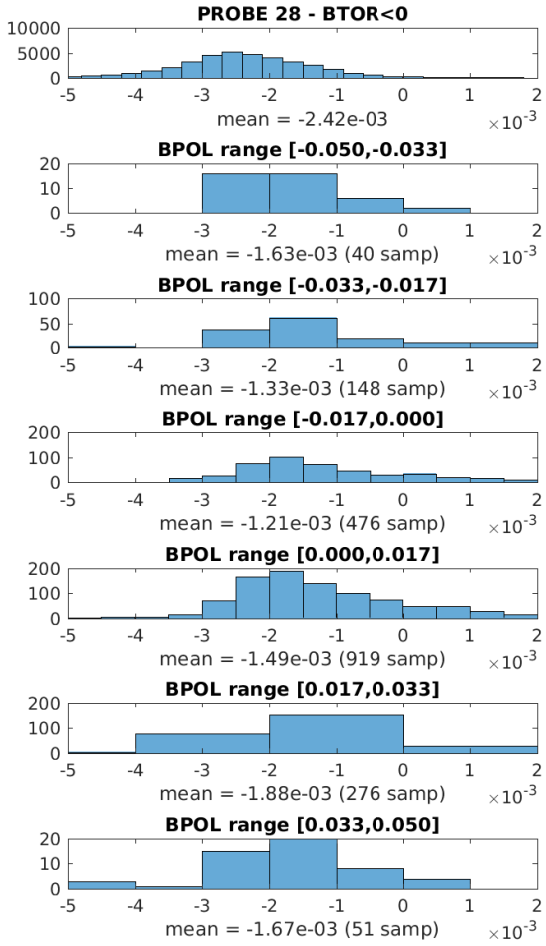

Figure 15. Error distribution as function of B_p for **probe 28**

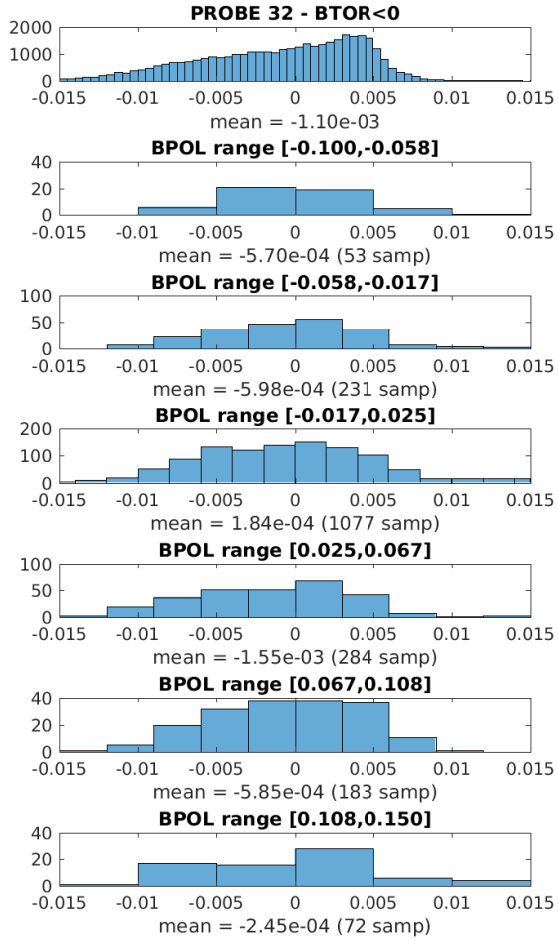

Figure 16. Error distribution as function of B_p for **probe 32**

Estimation of A_p and A_ϕ through regression Multivariable regression is applied to the model in Equation(55) in order to find the coefficients $(A_p + \epsilon_{cal})$ and A_ϕ for each probe. The graphs in Figure 17 and 18 graphically represents the results. The former plot shows that, for each probe, the value obtained

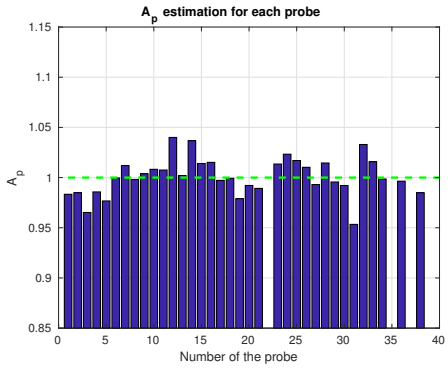

Figure 17. $(A_p + \epsilon_{cal})$ estimate for each probe

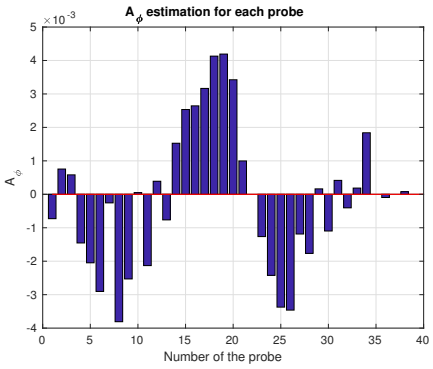

Figure 18. A_ϕ estimate for each probe

for $(A_p + \epsilon_{cal})$ is close to 1, as expected since the aim is to measure B_p. No particular trend due to the position of the probes is found for $(A_p + \epsilon_{cal})$. The fluctuations around 1 could be caused for example by a slight misalignment of the probes or by an inaccuracy at the stage of electronic amplification.
Regarding instead the estimation of the coupling with toroidal field, the plot shows that it varies both in sign and magnitude from one probe to another.
In particular it is negative for most of the probes labelled with numbers 3 to 13 and 23 to 30, and positive for those in the range 14 to 21. The position of the probes is shown in Figure 19, reporting a cross section of TCV.
By considering together the distribution of error as a function of B_p and the position of the probes, it is possible to see that the error is positive for the probes located in the region where the poloidal field is negative and negative for those in the region where it is positive. In order to confirm this theory, the mean B_p fiels is plotted, appropriately rescaled and superimposed to the graph with the mean of the errors for each probe. As shown in Figure 20 the trend followed by the mean of the calibration error and the mean of the poloidal field are strongly related. This finding refutes the initial assumption, made in section 4.1, that the error due to the toroidal field is not

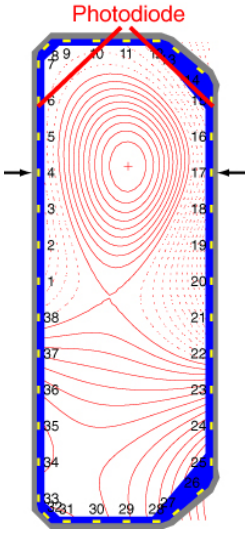

Figure 19. Magnetic probes distribution in TCV

influenced by the poloidal field.
An argument consistent with this result is represented by
the fact that the poloidal field is directly dependent on the plasma current I_p and, in turn, the plasma current changes if a variation of the toroidal field occurs. Therefore there is a dependence between the toroidal and the poloidal field which can explain why the parasitic error due to the toroidal field is influenced by the behaviour of the poloidal one.
Furthermore, it should be underlined that the multivariable regression has been done with two explanatory variables : B_p and B_ϕ. However, the latter can have only two possible values, the positive and the negative one, and the large majority of the samples are related to a the negative one. Therefore, one could deduce that one of the two explanatory variables, B_ϕ, behaves nearly as it was constant and consequently the multivariable regression is reduced to a simple linear regression. In order to prove this conclusion, in the regression algorithm the vector containing the values for B_ϕ was substituted by a vector of ones, leading to the same outcome obtained with the original input, as shown in Figure 21.
Consequently the model expressed in Equation (55) can be corrected as :

$$X = (A_p + \epsilon_{cal} + A_\phi \cdot B_\phi)B_p \tag{57}$$

Finally, a further improvement of the analysis could be implemented by weighting the contribution of the measurement for the positive and negative values of B_ϕ according to the frequency of each values, thus by dividing them by the number of samples. This would allow to exploit an actual multivariable regression and to find to what extent the parasitic error is dependent on the poloidal field.

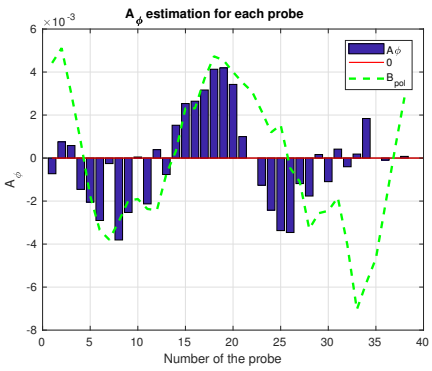

Figure 20. A_ϕ estimate for each probe with B_ϕ field

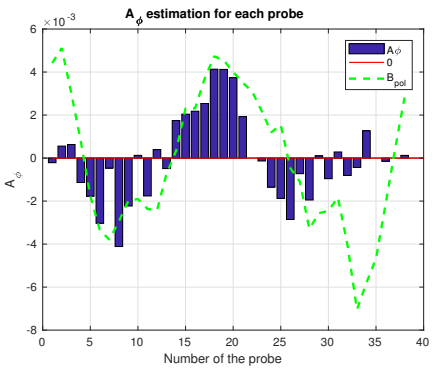

Figure 21. A_ϕ estimate for each probe with B_ϕ set to 1

These findings have shown that the error on the toroidal field affects the estimate of the error due to the poloidal field. Hence, in order to investigate the

contribution due to B_p only, the B_ϕ vector is set to zero in the regression. The model becomes, in this case :

$$X = (A_p + \epsilon_{cal})B_p \tag{58}$$

The estimate of $A_p + \epsilon_{cal}$ obtained with this regression is graphically shown in Figure 22.

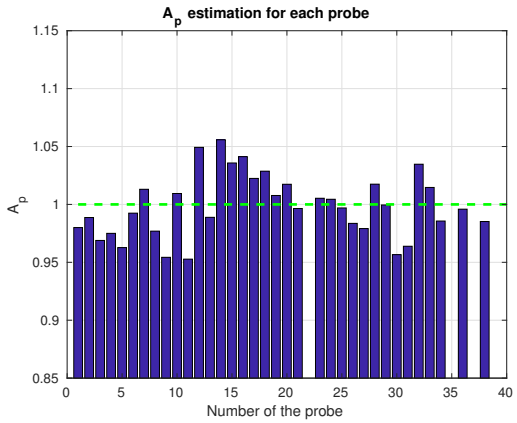

FIGURE 22. $(A_p + \epsilon_{cal})$ estimate for each probe with B_ϕ set to 0

As stated in the section **Error in the compensation of the toroidal parasitic contribution**, there is a connection between the distribution of the errors for the two classes of B_p and the mean error found through regression for each probe. Let us consider separately the four probes previously analyzed.
For probe 9, which has a positive mean for a positive B_ϕ and a negative mean otherwise, the estimation of A_ϕ is negative and with a magnitude large with respect to the other probes. On the contrary, for probe 15, which has a negative mean for positive B_ϕ and a negative mean otherwise, A_ϕ is found to have approximately the same magnitude but the opposite sign. Instead the probes 21 and 32, whose mean is positive or negative respectively for both classes of B_ϕ, are associated to a A_ϕ coefficient which is smaller in magnitude, with respect to the previous ones, and which is positive or negative respectively.
It as thus been proved that the greater the magnitude of the coupling represented by A_ϕ the bigger the difference between the means computed on the samples belonging to the two classes of B_ϕ. Additionally, the sign of A_ϕ determines whether, depending on the sign of the toroidal field, the coupling yields to a positive or negative error contribution on the measurement of B_p. It is interesting to observe how this estimation relates to the error distributions as function of the toroidal field displayed through histograms in Figures 5,6,7,8.

4.2 Error in poloidal current measurement

The distribution of the errors obtained as difference between the measurements and the fitted values for the poloidal current is shown, probe by probe to have a non zero mean. Unlike for the poloidal magnetic field, no parasitic coupling should be involved, thus the main source of inaccuracy is the calibration error. The model taking into account the calibration error can be expressed as :

$$X = (A_p + \epsilon_{cal})I_{pol} \tag{59}$$

As for the case of the poloidal magnetic field, the distribution of the poloidal current is continuous and it is divided in seven intervals in order to investigate whether the calibration error is proportional to the poloidal current. Proportionality in both sign and magnitude is investigated.
Since the distribution of the poloidal current varies significantly from one coil to another, different ranges are fixed for each coil. The most meaningful results for some of the coils are here presented.

Coil 18 OH2 The distribution of the errors with the corresponding mean value for each range is reported in Figure 23.
As evident from the histograms and from the mean values, the errors distributions are characterized by a negative mean when the poloidal current is negative, while they present a positive mean when the samples with positive I_{pol} are considered. However, for the samples lying in the positive tail of the distribution of I_{pol} (range $I_{pol} \in [15000A, 30000A]$), the inverse trend is found.
In Figure 24 the behaviour of the mean of the error has been plotted against the value of the poloidal current. From the plot it emerges that for values of I_{pol} up to approximately $I_{pol} = 1.3 \cdot 10^4 A$ the calibration error is proportional to the current, but for higher values of I_{pol} it gives a contribution opposite in sign and dramatically increased in magnitude. The linearly increasing part has been fitted with a line whose slope corresponds to the calibration error and is found to be :

$$\epsilon_{cal} = 1.68 \cdot 10^{-3} \tag{60}$$

Concerning the variance, by looking at the number of samples belonging to each interval as reported in Figure 23, it is possible to verify that for more populated ranges the variance is lower, and viceversa.

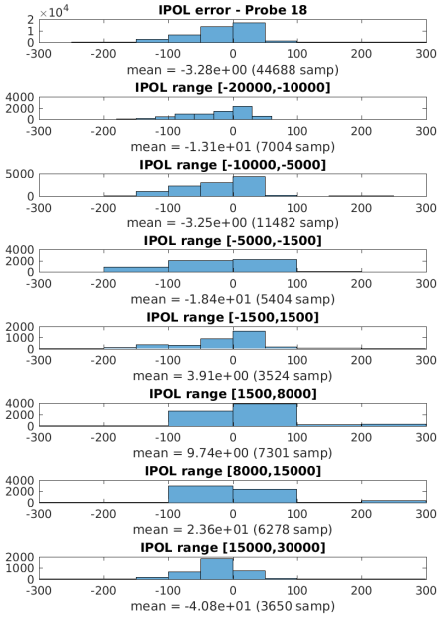

Figure 23. Error distribution for current coil 18

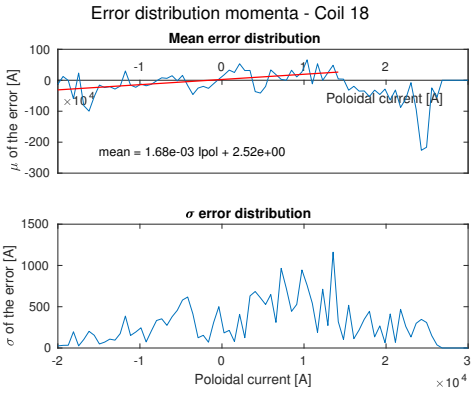

Figure 24. Error distribution for current coil 18

Coil 9 F1 The error distribution for the current in coil 9 has drawn our attention since, being characterized by the superposition of two distributions peaked around two different values, one negative and one positive, represented an occasion to investigate whether the two distributions correspond to different values of the poloidal current. The error trend is shown in histogram in Figure 25.
In order to detect a potential dependence of the error on the poloidal current, a 3D histogram, where the error is set on the x axis and the current on the y axis, is build. The histogram is shown in Figure 26, together with a 2D color map in which the intensity is associated to the number of samples. As already evident from Figure 25, it is possible to see that the error is mainly concentrated around its negative peak, which coincides with positive values of the poloidal current. The tails of the distribution, furthermore, are distributed with a rotation of an angle with respect to the current axis such that the tail towards more negative values for the error falls where there are more positive values for the current and viceversa. The second peak, instead, is barely visible in the right corner of the color map, and it lies in the quadrant corresponding to the negative values of I_{pol}. Therefore this proves that the calibration error is dependent on the poloidal current.

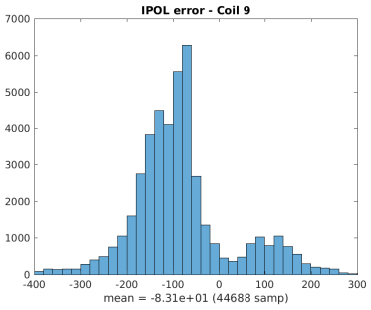

Figure 25. Error distribution for current coil 9

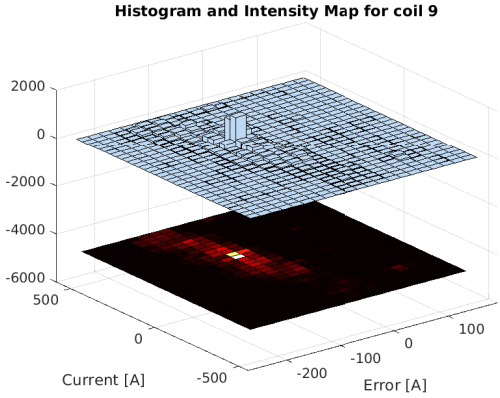

Figure 26. Error distribution for current coil 9

As done for coil 18, the measurements concerning coil 9 have been divided into different ranges according to the value of the poloidal current. Since a greater number of data is available, the number of intervals has been increased to 18. The histograms showing the distribution of error for each range are reported in Figure 28, where the mean value and the number of considered samples are displayed as well.
A clear trend is observed : in each range the errors are distributed with a peak that is shifted from positive to negative values as the I_{pol} increases from negative

to positive values. The mean of the distribution is positive for values of the current ranging from -1000 A to -300 A, and negative otherwise. From the data on the number of samples, it can be remarked that the range $I_{pol} \in [-600A, -300A]$ is more populated than the adjacent ones : indeed it corresponds, as found from the analysis of the 3D histogram, to the second peak of the error distribution. Similarly, the range $I_{pol} \in [100A, 100A]$, containing the largest number of samples, corresponds to the highest peak of the error distribution.

In Figure 27 the behaviour of the mean of the error has been plotted against the value of the poloidal current. From the plot it emerges that the calibration error has a linearly decreasing behaviour, inversely proportional to the current. The obtained curve does not intersect the current axis in 0, thus an offset is present. The curve has been fitted with a line, which is plotted over the mean graph. The slope of the fitted line corresponds to the calibration error and is found to be :

$$\epsilon_{cal} = -1.02 \cdot 10^{-1} \quad (61)$$

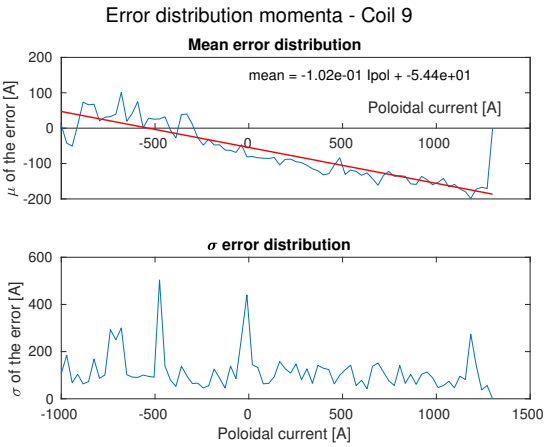

Figure 27. Error distribution for current coil 9

Concerning the variance, three spikes are found. The one in proximity of $I_p = 1200A$ is due to the lower number of samples available for the range. Instead the spikes around $I_{pol} = 0A$ and $I_{pol} = -500A$ cannot be explained through the population of the surrounding intervals nor by a sudden change in the mean, but their causes should be further investigated.

5 Suggestions for further developments

The described techniques employed to characterize the measurement errors for the poloidal magnetic field and the poloidal current can be systematically applied to the other measured quantities in TCV.

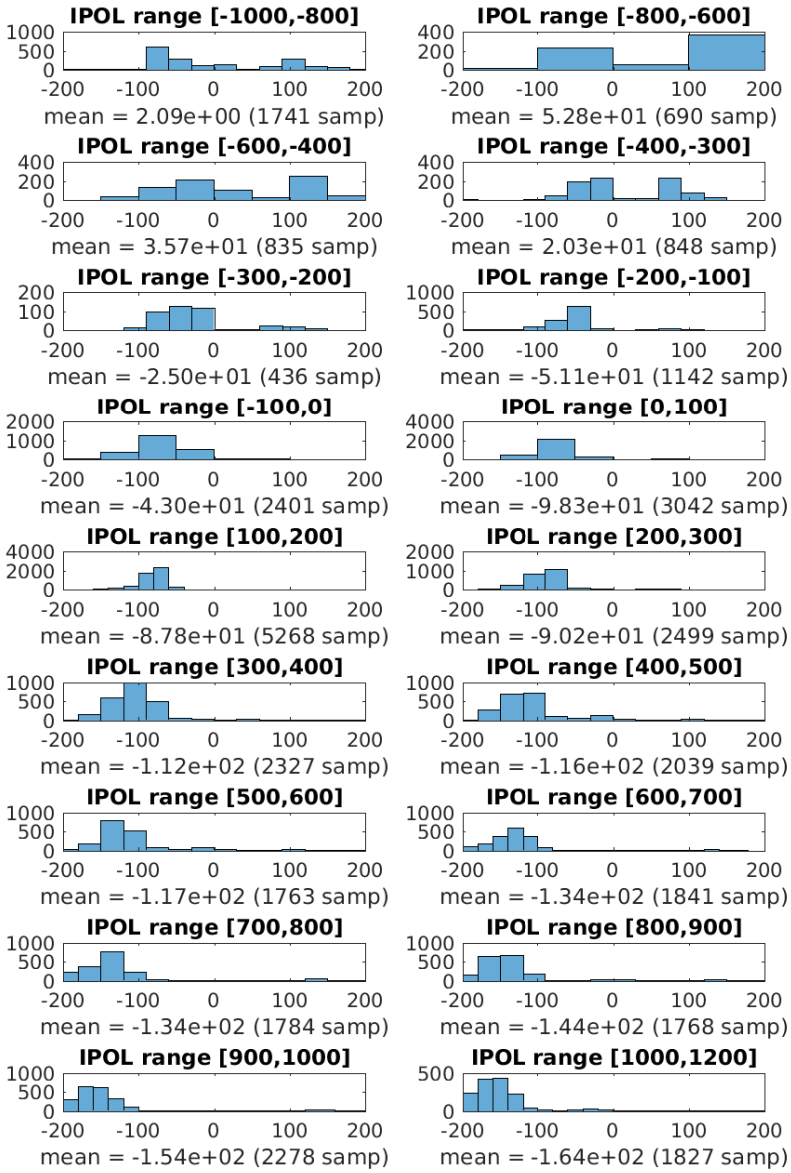

Figure 28. Error distribution for current coil 9 as function of the poloidal current

Bibliographie

MORET J.-M., et al., *Tokamak equilibrium reconstruction code LIUQE and its real time implementation*, Fusion Eng. Des. (2015)